THE ASTROPHYSICAL JOURNAL, 277:542–549, 1984 February 15

IMAGES IN THE ROCKET ULTRAVIOLET: PHOTOMETRY OF M101

JESSE K. HILL
Systems and Applied Sciences Corporation
AND
RALPH C. BOHLIN AND THEODORE P. STECHER
Laboratory for Astronomy and Solar Physics, Goddard Space Flight Center
Received 1983 May 13; accepted 1983 July 29

ABSTRACT

Three ultraviolet images of the Sc I galaxy M101 (NGC 5457) were obtained by a rocket-borne Ritchey-Chrétien telescope, using a microchannel plate image intensifier coupled to IIa-O film, giving an effective wavelength of 2250 Å, a bandpass of 970 Å, and about 10″ resolution over an 80′ field. Extreme Population I dominates in the UV in the form of OB/H II complexes. The digitized images were searched for discrete sources, subject to constraints on flux, profile shape, and distance between sources. Fluxes are given for 76 sources measured over 67″ boxes with a relative accuracy of 10%. Positions are accurate to 5″. Forty of the measured sources coincide with H II regions previously known from ground-based data, of which NGC 5471 is both the brightest and the most centrally condensed. About 20 are stars, while the rest are mostly fainter OB/H II complexes. The measured OB/H II complexes account for half the flux of the galaxy in our bandpass.

Large-scale spiral structure was investigated using azimuthal and radial profiles, as in previous optical studies. Prominent peaks on the azimuthal profiles can generally be identified with individual OB/H II complexes. A comparison with optical results shows that the colors of the disk and spiral arm components do not vary significantly with radius, and that the arm-to-disk ratio is a factor ~3 higher in the UV than in the visible.

Subject headings: galaxies: individual — galaxies: photometry — galaxies: stellar content — nebulae: H II regions — sky photographs — ultraviolet: general

I. INTRODUCTION

Ultraviolet imagery of spiral galaxies is a sensitive probe of the large-scale morphology of the star-forming regions and the associated interstellar dust. Comparison with images obtained at visual wavelengths is useful in estimating the relative ages of different structural features and in making comparisons with the predictions of theories of spiral galaxy structure and evolution, such as the density wave theory. We have chosen M101 (NGC 5457) as the first extragalactic target for our rocket-borne imaging Ritchey-Chrétien telescope because of the wealth of ground-based observations in existence at visual and radio wavelengths (see, e.g., Schweizer 1976; Israel, Goss, and Allen 1975; Allen and Goss 1979) and because of its large angular size (~30′). The results of an investigation of the abundance of dust in the outer regions of M101 based on the images obtained here have previously been published (Stecher *et al.* 1982). In the present paper, we describe the procedures for reduction and absolute calibration of the images obtained (§ II) and the results of an analysis in terms of discrete sources (§ III) and in terms of radial and azimuthal surface variations (§ IV). The conclusions are summarized in § V.

II. OBSERVATIONS AND DATA REDUCTION

a) Payload and Flight Data

The payload, which was launched from White Sands Missile Range at 5:00 UT 1979 May 21 on Astrobee 25.043, consisted of a 31.1 cm effective diameter f/5.6 Ritchey-Chrétien telescope with an electrostatically focused ITT microchannel plate image intensifier coupled to Kodak IIa-O film, as described by Bohlin *et al.* (1982). The bandpass was defined by the response of the CsTe photocathode, with a calcium fluoride filter to eliminate geocoronal Lyα emission. The vital statistics of the payload optics plus detector system are given in Table 1.

Three flight exposures of M101 were obtained, with exposure times 8 s, 20 s, and 60 s. Spatial resolution was limited by rocket pointing and stability to 10″ on the 8 s and 20 s exposures, and 10″ × 30″ on the 60 s exposure.

b) Preflight Bandpass Calibration

Figure 1 shows the relative response R per unit input energy flux as a function of wavelength, as determined from preflight laboratory calibration data. The entire rocket payload was enclosed in a vacuum tank and illuminated with collimated light from a hydrogen lamp and a scanning monochromator. A calibrated photomultiplier tube sampled the intensity in the input beam, while a second photomultiplier recorded a current proportional to the output from the microchannel plate phosphor. Maximum response for a flat spectrum source occurs at a wavelength of 2650 Å.

If one assumes that R is normalized to unity at the peak, the bandwidth, defined as the integral of R over wavelength, is 970 Å. The effective wavelength depends on the source spectrum and is defined as the mean wavelength weighted by the response function R times the source flux per wavelength interval. The effective wavelength of the bandpass for the flux distribution of NGC 5471, as determined by our *IUE* observations, is 2250 Å.

TABLE 1

INSTRUMENTAL PARAMETERS

Parameter	Value
Optics:	
Focal ratio	f/5.6
Effective primary diameter	31.1 cm
Collecting area	491 cm^2
No. of reflecting surfaces	4 (Al + MgF_2)
Plate scale	2.00 ± 0.002 arcmin mm^{-1}
Detector:	
Type	ITT Microchannel plate
Window	CaF_2
Cathode	CsTe
Diameter	40 mm
Output	Phosphor/Fiber Optics
Data	70 mm Kodak IIa-O
System resolution	80 μm (10″)
Flight:	
Date	5^h00 UT 21 May 1979
Place	White Sands Missile Range
Rocket	Astrobee 25.043
Pointing system	STRAP IV
Limit cycle	5″

c) *Reduction of Flight Data*

The steps followed in digitizing and reducing the image data to relative intensity were similar to those followed in the reduction of the Orion Nebula image data obtained on a previous flight of our instrument, as described by Bohlin *et al.* (1982). All flight frames and laboratory calibration images were digitized on a PDS 1010 microdensitometer, using a 20 μm square aperture rather than the 80 μm aperture used previously, resulting in 2048 × 2048 pixel density images. We corrected for drift of the PDS response with time by additively adjusting all densities in each scan line by a smooth function of scan line to give a uniform fog level for regions on the film outside the field of view. The images were box-averaged to 512 × 512 arrays of 80 μm pixels after application of the H and D curve.

The H and D curve, consisting of a 1024 element lookup table for the 10-bit PDS density digitization, was determined for densities less than about 1.5 from a series of flat field laboratory exposures taken with geometrically increasing exposure times. For higher densities, the H and D curve was determined by requiring that the three flight frames give consistent photometric results for the brighter sources. Vignetting and non-uniformities in cathode sensitivity were removed by dividing by a laboratory flat field exposure. The accuracy of the conversion to relative intensity and flat fielding is estimated from the reproducibility of the sky level and the brightest sources to be ±10% over the density range 0.5 to 3.0, or a dynamic range of about 100 in exposure.

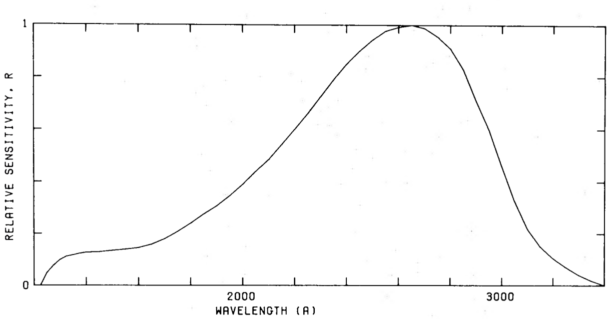

FIG. 1.—Relative response per unit input energy flux as a function of wavelength.

We determined the absolute calibration using the method described by Bohlin *et al.*, in which UV spectra of standard sources which appear on the flight images are integrated over the bandpass to determine an average flux at the effective wavelength. In this case the standards used were the H II region sources NGC 5455, 5461, and 5471, as observed by us with the *IUE* SWP and LWR cameras in low dispersion. Photometry of these three sources on the flight exposures then determined the conversion factor between relative intensities and flux in absolute units. We estimate the accuracy of the calibration to be ±15%.

The average sky brightness was determined to an accuracy of about 10% on each frame as the mean of measurements taken along the boundaries of a square box about one degree on a side centered on the optical axis. For the 8 s and 60 s exposures the resultant sky brightness was 1.3×10^{-8} ergs cm^{-2} s^{-1} $Å^{-1}$ sr^{-1}, and is mainly due to atmospheric emission by NO. The sky is somewhat brighter on the 20 s exposure because it was taken while the rocket was at a lower altitude. The sky brightness was subtracted from each pixel in each image before performing any further photometric measurements.

The data reduction steps described converted the three M101 flight exposures to 512 × 512 matrices of the specific intensity above sky in absolute units, averaged over 80 μm pixels, corresponding to 9″.6 for a plate scale of 2′.0 mm^{-1}. In order to make the large amount of data more manageable, a method of characterizing the reduced digital images using a relatively small number of parameters had to be found. Obviously many possible methods exist. We chose to explore two complementary approaches for condensing the information present:

1. Measurement of positions and fluxes of all discrete sources subject to a set of search criteria.
2. Measurement of surface brightness variations over angular scales comparable with the dimensions of the large scale structures in M101.

III. DETERMINATION OF FLUXES AND POSITIONS OF SOURCES

a) *Summary of Previous Work*

Most of the discrete sources present on rocket UV images of spiral galaxies are expected to be OB/H II complexes. Many surveys of H II regions in spiral galaxies based upon optical data may be found in the literature. Previous work in this field has been reviewed by Hodge (1982). Most of it has been based on nonphotometric plate material and has not used digital techniques for the identification of sources or position measurement. Hodge (1969) has published an atlas of H II regions identified on Hα Schmidt plates for 20 nearby spiral galaxies, including M101.

Our work is the first in which a calibrated far-UV image has been surveyed for OB/H II region sources using digital techniques. The use of source identification and measurement techniques appropriate for digitized plate material has been discussed by Herzog and Illingworth (1977) and Kron (1980).

TABLE 2

UV SOURCE PARAMETERS

No. (1)	Identification (2)	R.A. (3)	Decl. (4)	$F_{uv} \times 10^{14}$ (ergs cm^{-2} Å^{-1} s^{-1}) (5)	Pt. Frac. (6)
1	star	$13^h59^m48^s.0$	54°50′ 8″	0.46	0.96
2	star	14 0 6.2	54 45 24	0.54	0.95
3	AG1	14 0 8.2	54 30 46	0.29	0.79
4	AG2	14 0 14.3	54 37 39	0.15	0.43
5	OB/H II	14 0 24.1	54 32 59	0.22	0.36
6	AG4	14 0 26.2	54 46 0	0.56	0.92
7	OB/H II	14 0 29.8	54 40 38	0.51	0.37
8	H172, H175, H180, H181	14 0 33.7	54 32 18	1.10	0.33
9	H171, H174, H178, H179, H182	14 0 33.8	54 34 34	0.74	0.25
10	H170, H173, H177	14 0 36.0	54 36 25	0.64	0.24
11	H176	14 0 37.4	54 37 52	0.33	0.15
12	H163, H166	14 0 38.0	54 41 57	0.60	0.29
13	N5449, H157, H162, H164	14 0 40.8	54 34 15	1.40	0.42
14	OB/H II	14 0 40.9	54 28 11	0.23	0.37
15	N5447, H151, H152, H153, H155, H156, H159, H160, H161	14 0 42.0	54 30 46	2.70	0.55
16	OB/H II	14 0 43.7	54 43 1	0.36	0.33
17	H148, H149	14 0 46.8	54 39 56	0.24	0.24
18	N5451, S8, H146, H147	14 0 49.7	54 36 15	0.83	0.43
19	OB/H II	14 0 53.3	54 43 26	0.38	0.34
20	H142	14 0 56.6	54 37 56	0.53	0.27
21	H143, H144	14 0 57.8	54 34 33	0.46	0.16
22	OB/H II	14 1 0.0	54 39 37	0.26	0.28
23	OB/H II	14 1 0.3	54 43 6	0.33	0.21
24	H137, H138, H147	14 1 1.6	54 29 21	0.88	0.28
25	H131, H132, H136	14 1 2.4	54 32 17	1.20	0.17
26	OB/H II	14 1 4.4	54 35 3	1.10	0.19
27	H126, H127	14 1 6.4	54 40 45	0.38	0.29
28	OB/H II	14 1 7.1	54 46 0	0.30	0.32
29	S5, H124, H125	14 1 8.9	54 36 50	0.74	0.25
30	H120, H122, H123	14 1 10.3	54 32 46	1.40	0.33
31	H113, H118, H121	14 1 13.6	54 37 50	0.81	0.14
32	N5455, S10, H116, H119	14 1 14.3	54 28 54	1.80	0.67
33	OB/H II	14 1 15.5	54 34 22	1.60	0.28
34	OB/H II	14 1 17.4	54 41 41	0.34	0.19
35	S1, H105	14 1 20.9	54 36 15	1.30	0.23
36	H93, H96, H100	14 1 22.9	54 37 59	1.20	0.19
37	H82, H84, H88	14 1 26.1	54 32 14	1.60	0.33
38	H80, H99	14 1 26.6	54 35 18	1.50	0.20
39	Goss I	14 1 27.8	54 50 0	0.41	0.38
40	H94	14 1 28.2	54 36 29	1.40	0.19
41	H74, H76, H79, H81, H85	14 1 28.8	54 33 16	1.10	0.13
42	H75, H77, H78, H83, H86	14 1 30.7	54 31 35	1.30	0.17
43	OB/H II	14 1 32.5	54 37 53	0.89	0.14
44	S6, H63, H70, H72	14 1 37.9	54 39 45	1.10	0.34
45	H62, H68	14 1 39.0	54 31 37	1.10	0.19
46	H53, H57, H58, H60, H71	14 1 39.9	54 34 24	1.60	0.19
47	H47	14 1 41.4	54 33 8	1.30	0.28
48	H43, H45, H46, H49, H51, H54, H59, H61	14 1 41.5	54 38 28	1.40	0.17
49	H29, H33, H35, H37, H42	14 1 45.7	54 36 36	1.30	0.16
50	H36, H41	14 1 45.9	54 31 49	1.70	0.37
51	OB/H II	14 1 49.9	54 41 33	0.18	0.32
52	OB/H II	14 1 50.8	54 46 6	0.32	0.28
53	N5461, S7, H15, H17, H19, H22, H23	14 1 55.1	54 33 26	1.90	0.51
54	H14, H18	14 1 55.4	54 38 8	0.28	0.25
55	OB/H II	14 1 57.6	54 43 51	0.39	0.38
56	H12, H13	14 2 0.8	54 34 13	0.52	0.20
57	AG7	14 2 3.2	54 23 30	0.62	1.02
58	OB/H II	14 2 4.3	54 41 58	0.31	0.31
59	N5462, H6, H7, H8, H9, H11	14 2 7.4	54 36 20	2.60	0.45
60	AG8	14 2 7.7	54 52 39	0.16	0.59
61	star	14 2 12.2	54 33 13	0.15	0.39
62	H1	14 2 13.5	54 37 49	0.42	0.16

TABLE 2—*Continued*

No. (1)	Identification (2)	r.a. (3)	Decl. (4)	$F_{uv} \times 10^{14}$ (ergs cm^{-2} Å^{-1} s^{-1}) (5)	Pt. Frac. (6)
63	AG9	14 2 16.6	54 32 34	0.17	0.45
64	S12	14 2 25.7	54 39 45	0.71	0.66
65	star	14 2 30.3	54 41 48	0.18	0.31
66	AG10	14 2 35.9	54 33 42	0.41	0.86
67	AG11	14 2 39.7	54 53 36	5.80	0.98
68	N5471, S13	14 2 43.5	54 38 7	2.90	0.80
69	star	14 2 56.0	54 35 28	0.18	0.51
70	star	14 3 4.4	54 54 25	0.07	0.78
71	star	14 3 16.6	54 34 41	0.07	0.78
72	star	14 3 20.9	54 45 47	0.11	0.92
73	star	14 3 26.4	54 27 1	0.07	0.82
74	N5477	14 3 48.8	54 42 3	0.69	0.34
75	star	14 3 52.2	54 32 59	4.90	0.99
76	star	14 4 2.4	54 36 48	0.13	0.88

b) Source Searching

Source fluxes and positions were found automatically using software written for the IBM 3081 at GSFC. The flat fielded 60 s intensity image was first searched for local maxima over a square box of length about 30′ centered on the nucleus.

Flux measurements were performed for 3 × 3, 5 × 5, and 7 × 7 pixel apertures, giving F_3, F_5, and F_7 for each source. Measurements of stars show that for point sources $F_5/F_3 = 1.8$ and $F_7/F_5 = 1.2$. Given F_5 and F_3, with $F_5/F_3 > 1.8$ for extended sources, the source structure within the five pixel aperture can be modeled as a point source plus a uniform background. The model point source contributions to the measured fluxes F_5 and F_7 were then determined for each of the 400 potential sources. The source list was pruned by deleting all sources whose fractional point source contributions to F_5 were less than 0.20, or whose model point source flux contributions to F_7 were less than 5.0×10^{-16} ergs cm^{-2} Å^{-1} s^{-1}. Finally, all sources less than five pixels (48″) from the nearest brighter source were deleted.

c) The Final List of Sources

After pruning, 76 sources remained on the 60 s exposure. The shorter exposures were used only in the determination of the H and D curve at the higher densities and in the estimation of the probable errors in the resulting photometry. For each source we determined, and report here as "F_{uv}" in Table 2, the flux F_7 in a 7 × 7 pixel aperture (67″). As explained earlier, the effective wavelength depends on the spectrum of the source, and is near 2250 Å for OB/H II complexes. In column (6), Table 2 also gives the fraction of the flux accounted for by the point source in the simple source structure models discussed above. This fraction is useful mainly to assess the degree of central condensation of the sources. For the brighter stars this fraction is very near unity, as expected. Seven by seven pixels was chosen as the optimum aperture for our final measurements from a consideration of the rate at which the measured flux of point sources increases with aperture. More than 95% of the flux from a point source is contained within a 7 × 7 pixel box, while 5 × 5 pixel apertures miss 20% of the flux of a point source.

The effect of varying the threshold parameters in each of the source inclusion criteria was explored. The number of sources retained is most sensitive to the minimum model point source flux. Although the final value of this parameter could have been decreased by a factor of 2 without using pixels with densities on the toe of the H and D curve, 15 of the 20 additional sources surviving the pruning of the list would have been faint foreground stars near the periphery of the field.

Because the size of the aperture over which the photometry was done is 7 × 7 pixels, while the minimum distance allowed between sources is five pixels, some sources overlap. Increasing the minimum distance between sources to seven pixels only reduced the number of sources to 72, so source overlap is unimportant. Decreasing the minimum point source fraction in a 5 × 5 pixel aperture to 0.15 only increased the number of accepted sources to 80. The final values of the search parameters thus seem to be well matched to the sensitivity and resolution of our images.

d) Astrometry and Source Identification

Although our field of view contains the stars SAO 28976 and SAO 28988, we could not use them in an accurate determination of the plate constants because their images are large and saturated, even on the 8 s exposure. Fortunately, our field also contains 11 stars with positions measured to 1″ accuracy by Allen and Goss, eight of which are visible on our longest exposure. These eight stars were used to determine a plate solution which allowed us to compute the 1950.0 equatorial coordinates for the centroids of each of the 76 sources reported in Table 2 to an accuracy of about 5″, or about 0.15 of the FWHM of a point source.

The majority of the sources detected within 10′ of the nucleus are expected to be OB/H II complexes. Seven of the UV sources have positions within 10″ of radio positions reported by Israel, Goss, and Allen (1975) and Viallefond, Allen, and Goss (1981) which also correspond to objects in the NGC catalog; their NGC numbers are given in column (2) of Table 2 with the prefix N. There are 37 UV sources with one or more Hodge H II regions located within 33″ of their centroid positions and thus nominally within a 67″ (seven pixel) box centered on the UV source. These sources are identified by a series of H-numbers in column (2). A total of 113 Hodge H II regions lie within 33″ of UV sources. Seven of the UV sources correspond to H II regions studied spectroscopically by Searle (1971). These sources are denoted by S-numbers in column (2). UV source 39 corresponds within 5″ with the prominent H II region Goss I (Allen, Goss, and Van Woerden 1973). Source 74 may be identified with the companion dwarf galaxy NGC 5477. The eight stars used in determining the plate solution, whose positions were tabulated by Allen and Goss (1979), have AG numbers entered in column (2).

Of the remaining 27 sources not coincident in position to within 33″ with sources in any of the catalogs searched we have entered either "star" or "OB/H II," based on inspection of the optical photograph of Sandage and Tammann (1974) to determine whether the source appears stellar or extended. Eleven of these sources appear to be stellar.

e) *Results of Source Photometry*

The two brightest sources in Table 2 are source 67 and source 75, both of which are foreground stars. The five next brightest sources are the prominent OB/H II complexes NGC 5471, 5447, 5462, 5461, and 5455. NGC 5471 is remarkable in that it is the brightest of all the OB/H II complexes, and also the most centrally condensed, with a flux at 2250 Å of 2.9×10^{-14} ergs cm^{-2} Å^{-1} s^{-1} and a computed point source fraction of 0.80.

The total flux of M101 averaged over our bandpass was determined by summing all pixels within a radius of 12′ from the nucleus which were not contaminated by foreground stars, giving a result of 1.1×10^{-12} ergs cm^{-2} Å^{-1} s^{-1}. A fraction 0.48 of this flux is accounted for by the total of all the nonstellar sources in Table 2 within 12′ of the nucleus. The five brightest nonstellar sources account for 0.10 of the flux of the galaxy.

Figure 2 (Plate 5) shows the region of the 60 s exposure searched for sources, with boxes indicating the 67″ integration apertures corresponding to each of the sources appearing in Table 2. The fact that half of the UV flux of the galaxy is accounted for by the OB/H II complexes of Table 2 means that in our bandpass the flux from the galaxy is dominated by the extreme Population I.

IV. UV STRUCTURE OF M101 ON LARGE SCALES

a) *Summary of Previous Work*

Many discussions of the large-scale photometric structure of disk galaxies exist in the literature. The early work, based on microphotometer tracings of photographic plates and photoelectric aperture photometry, was summarized by de Vaucouleurs (1959), who showed that radial surface brightness variations of many disk galaxies can be described as the superposition of a spheroid component, with a profile similar to that of an elliptical galaxy, and a disk component, with an exponential variation of surface brightness with radial distance. Freeman's (1970) study of the nature of the exponential disk has been particularly influential on subsequent research. Schweizer (1976) was the first to use digitized photographic images to study the spiral structure of several well-known bright spiral galaxies, including M101, at visual wavelengths. He also determined the radial variation of the disk and arm components. Unlike previous workers, he differentiated between the old disk population and the young Population I, which dominates in the spiral arms. Talbot, Jensen, and Dufour (1978) utilized methods similar to those of Schweizer in a study of the spiral galaxy M83. Kormendy (1977), Burstein (1979*a*, *b*), and Boroson (1981) used digitized photographic images to study the spheroid and disk surface brightness structures in compact S0, normal S0, and spiral galaxies, respectively. In this section we follow the procedure described by Schweizer to study the surface brightness variations of the disk component with radius and the variation of the spiral arm component with radius and azimuthal angle.

b) *Procedure for Spiral Binning*

Computation of the surface profiles in radius and azimuth began with the assignment of each pixel of the reduced 60 s image to one of a grid of cells, whose shapes were chosen to mirror the observed symmetry of M101. The plane of the galaxy was divided into circular annuli, with each annulus further subdivided into 72 cells subtending azimuthal angles of 5°. The azimuthal cell boundaries were logarithmic spirals, $r = r_0 \exp(\varphi \tan i)$, where i is the pitch angle of the spiral arms and φ is the azimuthal angle increasing in the direction of galactic rotation, assuming the spiral arms are trailing. The azimuthal angle was measured with respect to an axis intersecting the nucleus at position angle 170°. Following Schweizer, we have set $i = 26°$. Although some of the brightest H II regions (e.g., NGC 5461, 5462, and 5447) lie along spiral arms which approximate logarithmic spirals of this pitch angle for a limited range of radius and azimuth, other bright sources (e.g., NGC 5471 and 5455) do not appear to lie along any definite spiral arm at all. M101 does not fit well the spiral structure grand design ideal, which consists of two prominent spiral arms which can be traced over a large range in radius and azimuth. Nevertheless, in order to facilitate comparisons with Schweizer's results, we adopt the same pitch angle, as well as the assumption that the galaxy is face on, so no inclination dependent corrections are made to intensities or the shapes of the cells.

c) *Radial Variation of Disk and Arms*

Schweizer distinguished between the spiral arm and old disk populations by defining the disk surface brightness I_D at any radius as the mean of the two minimum surface brightness measurements among the 72 cells at that radius, with the stipulation that the two cells averaged be at least 90° apart in azimuth and that neither be along a prominent dust lane. Applying this definition of the disk to images taken in three optical bandpasses, Schweizer concluded that the color of the old disk population does not vary with radius.

Figure 3 shows the variation of I_D with radial distance from the nucleus for our UV data, adopting Schweizer's definition of the disk. We have fitted an exponential curve of the form $I = I_0 \exp(-\alpha r)$ to the UV disk in the interval 2.4 kpc $< r <$ 18.4 kpc, resulting in a scale length α^{-1} of 4.53 ± 0.50 kpc, where the quoted error is the 2 σ error of the fit. We have computed radial distances using the distance to M101 of 7.2 Mpc determined by Sandage and Tammann. Schweizer reports a value of 4.11 kpc for the exponential scale length of the disk in his O bandpass image. His conclusion that the color of the disk component does not vary with radius can thus be extended to include our rocket UV bandpass as well, since the difference in scale lengths does not appear to be statistically significant. Again following Schweizer's procedure,

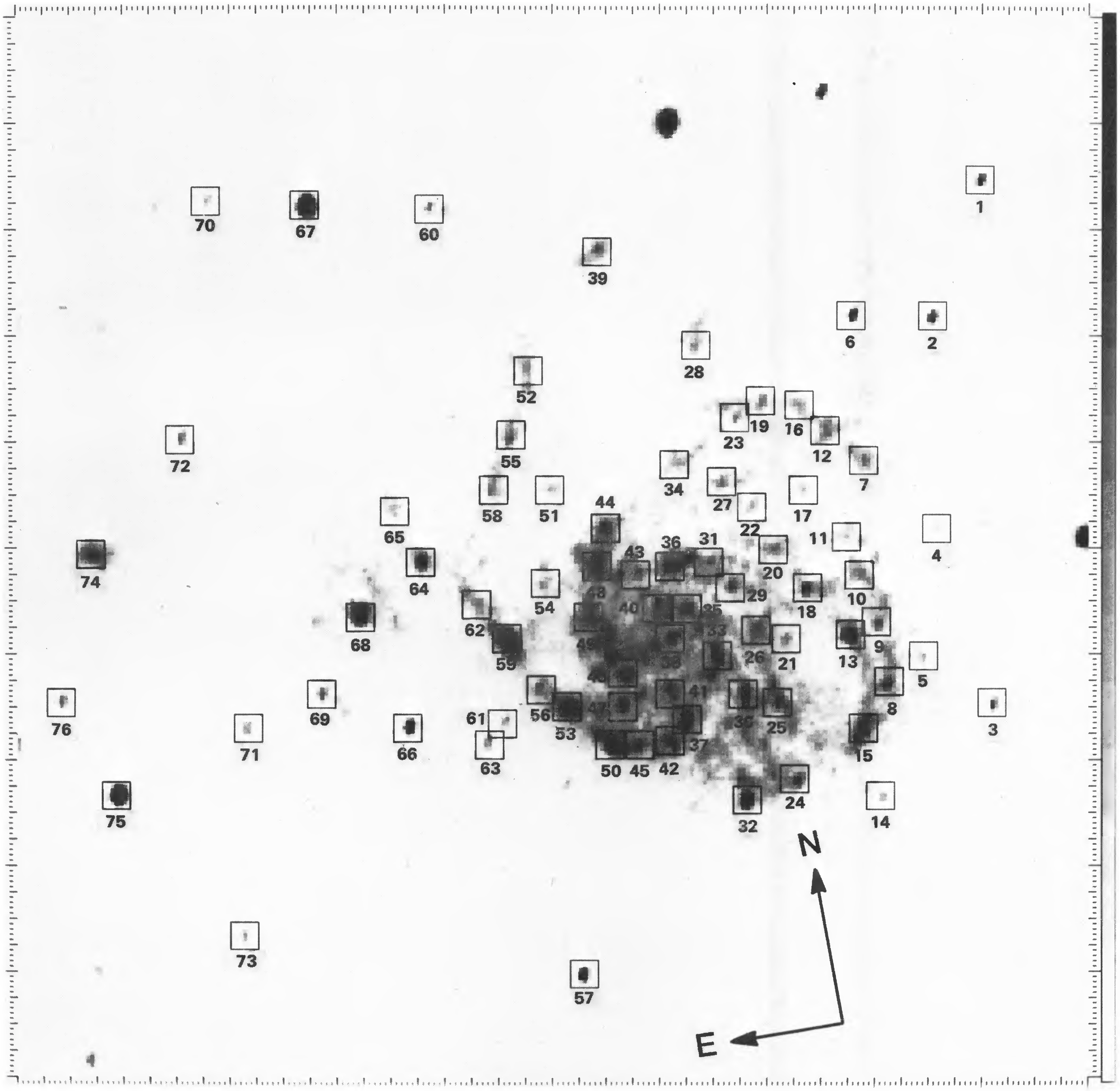

FIG. 2.—60 s exposure of M101 with boxes used in source photometry indicated along with the source numbers from Table 2. The boxes are 67″ on a side.

HILL *et al.* (*see* page 546)

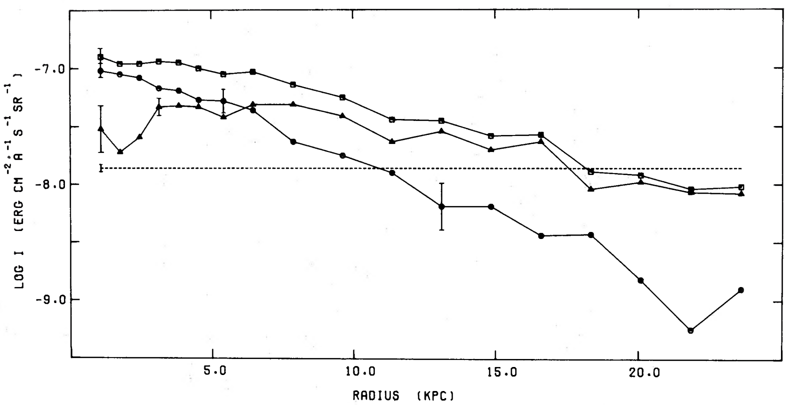

FIG. 3.—Radial UV surface brightness profiles. The total surface brightness, arm surface brightness, and disk surface brightness are indicated by the squares, triangles, and circles, respectively. The sky level is indicated by the dashed line. Error bars reflect the scatter between different exposures.

we define the arm surface brightness I_A at a given radius to be the average excess surface brightness above the (assumed) axisymmetric disk. The arm surface brightness, so defined, is also plotted in Figure 3. We find that although I_A appears to peak at a radial distance of about 6 kpc, I_A/I_D increases approximately linearly with radius, again consistent with Schweizer's results. For a sample of six spiral galaxies, he reports values of (I_A/I_D) for his O bandpass of about 0.2 for $r = 3$ kpc and about 1.0 at $r = 15$ kpc. He also states that the same approximately linear dependence of arm-to-disk ratio with radial distance holds for his B_3 and U bandpasses, with arm-to-disk ratios which are larger by factors of 1.22 and 1.63, respectively. For our UV bandpass we find an arm-to-disk ratio of 0.69 at $r = 3.2$ kpc and a ratio of 3.1 at $r = 14.9$ kpc, larger by a factor of 3.2 than for Schweizer's O band data (cf. his Fig. 8). It is this increase in I_A/I_D which accounts for the increasingly blue color of spiral galaxies with increasing distance from the nucleus. The fraction of the total light coming from the arms is 0.67 for our UV bandpass compared with 0.25, 0.28, and 0.37 for Schweizer's O, B_3, and U bandpasses, respectively.

An exponential fit to the total surface brightness (arms plus disk) gives a scale length of 7.1 kpc for our UV bandpass, where the fit is over the same radial distance interval as the fit to the disk. Schweizer reports a corresponding scale length of 5.28 kpc for his O bandpass data. The shallower falloff with radial distance in our data is a natural consequence of the larger I_A/I_D for our bandpass, and the fact that the arms dominate the disk for $r > 7$ kpc. Note that the fact that I_A/I_D scales approximately linearly with radius for all four bandpasses strongly suggests that the arm colors, like the disk colors, do not vary significantly with radial distance over the wavelength range 2250 Å (our UV bandpass) to about 6500 Å (Schweizer's O bandpass).

Although we have not attempted a formal decomposition of the radial surface brightness profiles into spheroid and disk components (as done by, e.g., Kormendy), it is clear from an inspection of the profiles that any spheroid component, if present at all, is very weak in the UV. If anything, there is a slight deficiency of flux relative to the extrapolated disk for $r < 2.4$ kpc. Schweizer's radial profiles for the disk in his O bandpass and the arms in his B_3 bandpass also do not show any evidence for an excess surface brightness at small radial distances that could be attributed to a significant spheroid component. This is not surprising since M101 is an Sc I galaxy, which would not be expected to have a prominent spheroid component.

d) Azimuthal Variation of Disk and Arms

Plots of the azimuthal surface brightness variations for each radial bin are presented in Figure 4, which can be compared with the azimuthal plots corresponding to Schweizer's U, B_3, and O bandpasses in his Figure 5*d*.

The azimuthal plots of Schweizer also show the increasing contrast of the spiral arms above the disk with decreasing effective wavelength from O to B_3 to U. The increasing constrast of the spiral arm features above the disk with increasing radial distance is readily apparent in all three of Schweizer's bandpasses, as it is in our UV bandpass in Figure 4.

A high degree of correlation exists between the small-scale structure visible on azimuthal profiles in the UV and in Schweizer's bandpasses. It is especially striking that the trend of increasing amplitude with decreasing effective wavelength, which is apparent in Schweizer's Figure 5*d*, is continued on our UV profiles. We conclude that the fine structure on the azimuthal profiles is real and is due to the patchy distribution of recently formed hot stars in the arms. The increase of the arm-to-disk ratio with radius is apparent from the increasing contrast of the spiral arm features above the disk level with increasing radial distance in the azimuthal plots.

It is tempting to relate the observed photometric structure of spiral galaxies to the predictions of the density wave theory of spiral structure. Schweizer did this by modeling the intensity profile of a spiral arm assuming that stars are formed as a result of the gravitational collapse of interstellar clouds, triggered by passage through a spiral shock front, as discussed by Roberts (1969), Shu *et al.* (1972), and others. The models predict a steeply rising surface brightness profile marking the post-shock region, followed by a slow decline corresponding to the aging of the newly formed stars. The width would then provide an estimate of the post-shock azimuthal velocity of the newly formed stars, and would be expected to decrease with increasing radial distance as the corotation radius is approached. Schweizer found that although spiral arm profiles with the predicted asymmetry

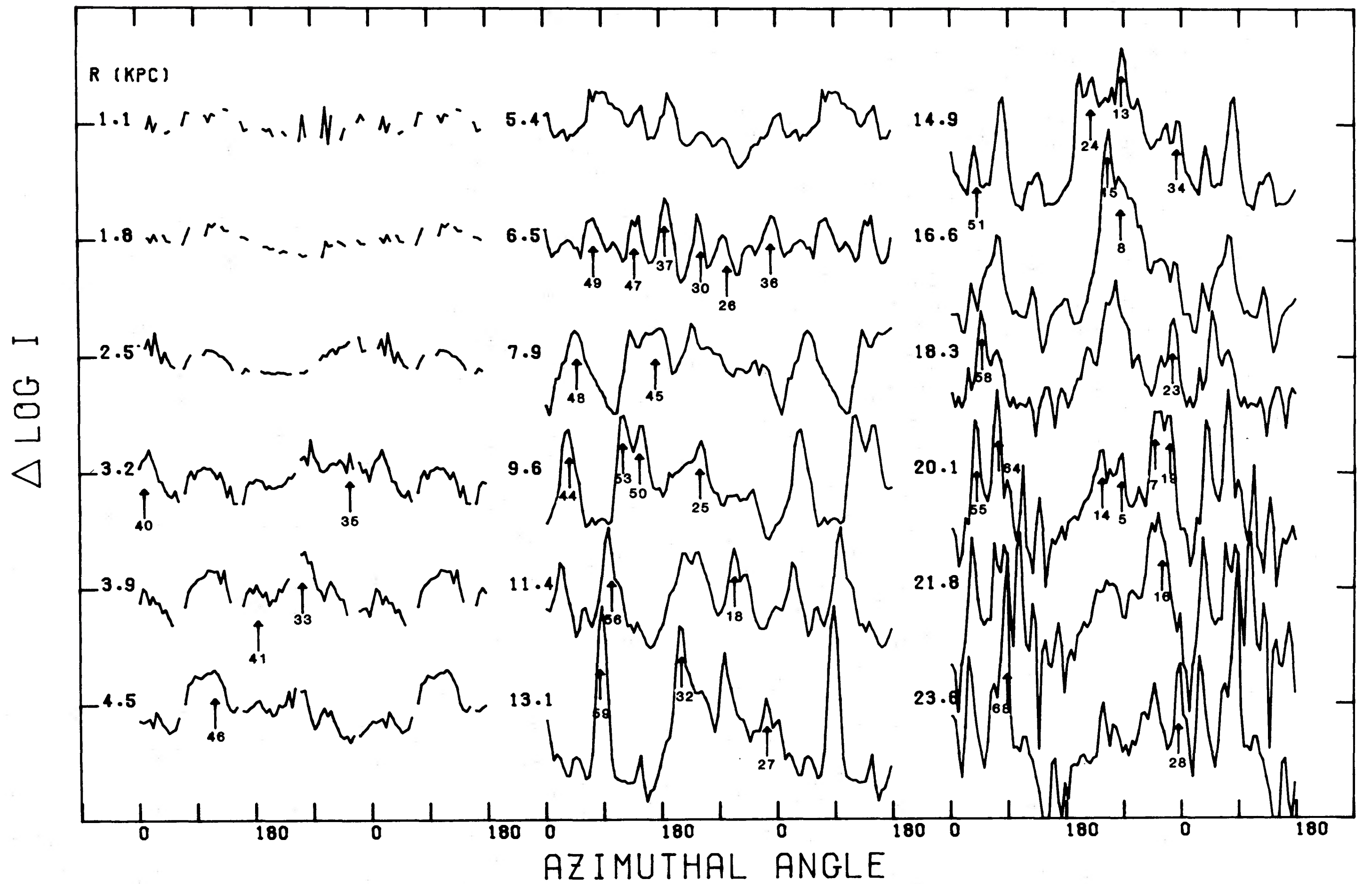

FIG. 4.—Azimuthal profiles of logarithmic UV surface brightness for each of the 18 radial bins. The mean radius in kpc is indicated for each profile at the tick mark corresponding to the mean surface brightness level for that radius. The distance between tick marks is equivalent to a factor of 10 in intensity. The positions of the centroids of prominent sources are indicated by arrows, along with source numbers from Table 2. The azimuthal angle is in degrees, with the range 0°–180° repeated.

exist, they are outnumbered by profiles which are symmetric or asymmetric in the opposite sense. Furthermore, the predicted decrease in the width of the profiles as corotation is approached is not found. Since the peaks on our UV azimuthal profiles generally correspond with peaks on Schweizer's profiles and with sources appearing on Table 2, we conclude that the shapes of the profiles are primarily determined by the internal structure and distribution in the arms of the individual OB/H II complexes. In addition, more recent theoretical work on the predictions of the density wave theory (e.g., Bash, Green, and Peters 1977), has shown that the assumption that newly formed stars will follow circular orbits with no significant radial velocity component is incorrect, and that the inclusion of this effect, together with a more realistic estimate for the width of the star-forming region, washes out the effects of the aging of the newly formed stars on the azimuthal profiles.

The increased width of the azimuthal profiles over the predictions of the models led Schweizer to ascribe the width of the profiles to the existence of spiral arms in the underlying disk. The existence of arms in the old disk population is required by the density wave theory, since the perturbation of the gravitational potential caused by the perturbed mass density in the spiral arms must be sufficient to cause a large nonlinear response in the gaseous component of the galaxy, and thereby result in the prominent extreme Population I seen in the spiral arms. Most of the mass is in the old disk population, so spiral arms in this population are required if the spiral pattern is to be self-sustaining. However, the amplitude of the spiral wave in the old disk population need not be large, in order to cause a large nonlinear response in the gaseous component of the galaxy (Shu, Milione, and Roberts 1973). Such low amplitude spiral arms in the older population would not necessarily be discernible photometrically in M101, since the arm regions are dominated by the extreme Population I.

The evidence for spiral arms in the disk population is strongest for Schweizer's images of NGC 3031 and NGC 5364, both of which have very regular spiral patterns. Interestingly enough, they also have low arm-to-disk surface brightness ratios compared with M101 (cf. Schweizer's Fig. 8). In the case of M101, it appears that the observed width of the spiral arm features can be accounted for by the patchy and somewhat irregular distribution of OB/H II complexes within the arms. The fact that the colors of the arms, as operationally defined by Schweizer, appear to be constant with radius for all the bandpasses studied suggests that the same extreme Population I dominates the arms over a wide wavelength range, which would account for the striking similarity between our azimuthal profiles and those of Schweizer.

V. SUMMARY OF CONCLUSIONS

Emission from M101 in our UV bandpass is dominated by extreme Population I, in the form of discrete OB/H II complexes. The five brightest sources, namely NGC 5471, 5447, 5462, 5461, and 5455, account for 0.10 of the total flux of M101 in our bandpass. NGC 5471 is the brightest OB/H II source and the most centrally condensed. The 57 OB/H II sources measured by us account for half the UV flux of the galaxy.

Comparison with the results of Schweizer show that the disk and arm colors are each approximately constant over the wavelength range 2250 Å to 6500 Å. The arm-to-disk ratio varies linearly with radius, and is a factor ~ 3 higher in the UV than in the visible.

Prominent peaks in our azimuthal profiles can be identified with individual OB/H II complexes. The similarity in the shapes of the azimuthal profiles constructed by us and by Schweizer suggests that the arm light is dominated by the extreme Population I in the visual bandpasses as well.

We thank the members of the Sounding Rocket Division of Goddard Space Flight Center and the Laboratory for Astronomy and Solar Physics including G. Baker, A. Stober, F. Richardson, J. Tebay, and W. Nichols, for their efforts in making Astrobee 25.043 a success. We thank Dr. Robert H. Cornett for microdensitometering the flight film and laboratory calibration exposures and for many useful discussions concerning data reduction and analysis, and Priscilla A. Struthers for assistance in preparation of the figures.

REFERENCES

Allen, R. J., and Goss, W. M. 1979, *Astr. Ap. Suppl.*, **36**, 182.
Allen, R. J., Goss, W. M., and Van Woerden, H. 1973, *Astr. Ap.*, **29**, 477.
Bash, F. N., Green, E., and Peters, W. L., III, 1977, *Ap. J.*, **217**, 464.
Bohlin, R. C., Hill, J. K., Stecher, T. P., and Witt, A. N. 1982, *Ap. J.*, **255**, 87.
Boroson, T. 1981, *Ap. J. Suppl.*, **46**, 177.
Burstein, D. 1979*a*, *Ap. J.*, **234**, 435.
———. 1979*b*, *Ap. J. Suppl.*, **41**, 435.
de Vaucouleurs, G. 1959, *Handbuch der Physik*, **53**, 311.
Freeman, K. C. 1970, *Ap. J.*, **160**, 811.
Herzog, A. D., and Illingworth, G. 1977, *Ap. J. Suppl.*, **33**, 55.
Hodge, P. W. 1969, *Ap. J. Suppl.*, **18**, 73.
———. 1982, *A.J.*, **87**, 1341.
Israel, F. P., Goss, W. M., and Allen, R. J. 1975, *Astr. Ap.*, **40**, 421.
Kormendy, J. 1977, *Ap. J.*, **217**, 406.
Kron, R. G. 1980, *Ap. J. Suppl.*, **43**, 305.
Roberts, W. W. 1969, *Ap. J.*, **158**, 123.
Sandage, A., and Tammann, G. A. 1974, *Ap. J.*, **194**, 223.
Searle, L. 1971, *Ap. J.*, **168**, 327.
Schweizer, F. 1976, *Ap. J. Suppl.*, **31**, 313.
Shu, F. H., Milione, V., Gebel, W., Yuan, C., Goldsmith, D. W., and Roberts, W. W. 1972, *Ap. J.*, **183**, 557.
Shu, F. H., Milione, V., and Roberts, W. W. 1973, *Ap. J.*, **183**, 819.
Stecher, T. P., Bohlin, R. C., Hill, J. K., and Jura, M. A. 1982, *Ap. J.* (*Letters*), **255**, L99.
Talbot, R. J., Jensen, E. B., and Dufour, R. J. 1979, *Ap. J.*, **229**, 91.
Viallefond, F., Allen, R. J., and Goss, W. M. 1981, *Astr. Ap.*, **104**, 127.

R. C. BOHLIN: Space Telescope Science Institute, Homewood Campus, Baltimore, MD 21218

J. K. HILL: Systems and Applied Sciences Corporation, 6811 Kenilworth Avenue, Riverdale, MD 20840

T. P. STECHER: Laboratory for Astronomy and Solar Physics, NASA Goddard Space Flight Center, Code 680, Greenbelt, MD 20771